Pore-Scale Modelling of Fluid-Rock Chemical Interactions in Shale during Hydraulic Fracturing

Hossein Fazeli[1,4*], Veerle Vandeginste[1,] Arash Rabbani[3], Masoud Babaei[3], Bagus Muljadi[2]

[1]School of Chemistry, University of Nottingham, University Park, NG7 2RD Nottingham, UK

[2]Department of Chemical and Environmental Engineering, University of Nottingham, NG7 2RD Nottingham, UK

[3]The University of Manchester, Department of Chemical Engineering and Analytical Science, Manchester, UK

[4]Institute of GeoEnergy Engineering, Heriot-Watt University, Edinburgh EH14 4AS, UK

ABSTRACT

During the hydraulic fracturing process in unconventional shale gas reservoirs, chemical interactions between the hydraulic fracturing fluid (HFF) and the shale rock could result in mineral precipitation and dissolution reactions, potentially influencing the gas transport by dissolving or clogging the fractures. The pore-scale distribution of the minerals, especially the highly reactive ones such as calcite, in the shale matrix can impact the structural evolution of the shale rocks. In the present study, a pore-scale reactive transport model is built to investigate the impact of the pore-scale distribution of calcite on the structural alteration of the shales. The alteration of the shales is caused by the barite precipitation, and the dissolution of calcite and pyrite. The simulation results show that the calcite dissolution leads to a permeability enhancement. The permeability enhancement for the shales with coarser calcite grains is more pronounced than that for the shales with finer grains of calcite. The results also indicate that the extent of the permeability enhancement is even more noticeable if the HFF is injected with a higher velocity. The fluid chemistry analysis indicates that the fluid pH for the shale with the fine grains of calcite is higher than that of the shale with the coarse calcite grains and that the injection of the HFF with a higher flowrate leads to the lower pH values. The calcite dissolution observed in the simulations mainly occurs near the inlet. For the shale with the finer calcite grains, barite precipitation also occurs mostly close to the inlet but for the shale with coarser calcite grains, barite precipitation extends more into the domain. This penetration depth increases when the HFF is injected with a higher velocity. In addition to the effect of the calcite distribution, we also used the pore-scale model to study the effect of the calcite content on the structural evolution of the shales. The results from these simulations showed that a higher calcite content can result in higher pH values, higher permeabilities, and also more barite precipitation in the domain.

KEYWORDS

Hydraulic fracturing; geochemical interactions; Pore-scale modelling;

1. INTRODUCTION

Natural gas is viewed as a reliable energy resource because it has high energy content and also emits less greenhouse gases such as CO_2 compared to the other fossil fuels[1]. In the US, a considerable amount of the increase in the natural gas production has been attributed to the production of gas from shale gas reservoirs[2]. Some of the formations in Europe, such as Posidonia, Alum, and Bowland–Hodder formations, are also believed to have economic potential for hydrocarbon production[3-5].

Because of their low permeability, shale gas reservoirs have to be stimulated by hydraulic fracturing so that the gas entrapped in the tight rocks can flow through the pathways generated during the fracturing process. The fractures in the rock are created by the injection of a fracturing fluid under high pressure. Once injected into the shale reservoir, hydraulic fracturing fluid (HFF) reacts with shale rock where, depending on the rock mineralogy and the different chemical components in the fracturing fluid, various chemical reactions might occur in the shale fractures and matrices during the fracturing process[6-12]. These geochemical reactions can change the transport properties of shales, affecting the gas production from shale gas reservoirs[6, 8, 9, 12-17]. For example, cases have been documented where the production rate decreased significantly within a short time after initial gas recovery from shale gas reservoirs, suggested to be caused by the precipitation of minerals in the fractures and the matrix of fractured shale reservoirs[7, 18]. The chemical reactions between HFF and shales can also influence the chemical composition of the produced water after the fracturing process[13, 14]. Therefore, understanding the chemical reactions between HFF and shales can help better predict the gas productivity and environmental impacts during hydraulic fracturing processes[15].

Various studies have investigated the effects of the HFF-shale chemical interactions on the hydrodynamic properties of shale rocks (such as porosity and permeability)[7, 8, 19-24] and on the flowback water chemistry[15, 17, 25-32]. Some of these studies have experimentally and numerically assessed the impact of HFF-shale chemical interactions on the alteration of the fracture-matrix interfaces at the pore-scale (μm-scale)[21, 22, 24]. Although formation of this altered layer is a pore-scale feature, it can have large-scale impacts on hydrocarbon recovery because the thickness of this altered zone can influence the transport (advection and diffusion) of hydrocarbons from matrices to fractures in shale formations[22]. A pore-scale parameter that control the structure of this altered zone (or the reacted shale in general) is the pore-scale distribution of the matrix-forming minerals, especially the highly reactive phases such as calcite. To our knowledge, there have not been studies systematically evaluating the impact of the pore-scale mineral distribution on the alteration of shale morphology during the HFF-shale chemical interactions. To fill this gap, we build a pore-scale reactive model to simulate the alteration of the shale morphology while reacting with the HFF. We choose pore-scale models because these models can resolve the pore-scale features such as mineral pore-scale distributions. The main focus of this study is to evaluate the effect of the pore-scale mineral distribution of calcite on the alteration of the shale morphology when the shale rock is exposed to an acidic HFF, which leads to the calcite dissolution. In addition to the effect of the pore-scale mineral distribution of calcite, we also use the built model to investigate the impact of the calcite content on the chemical alteration of the shale rocks at the pore-scale. Moreover, since the scale precipitation is another common mineral reaction during HFF-shale interactions, we also include the barite precipitation reaction (a common scale reaction in various fields[33-37] including hydraulic fracturing) in the simulations and will investigate how different calcite mineral distributions can impact the location of barite precipitates. We perform these simulations under different transport (flow velocity) conditions. The details of the model setup is discussed in the following section.

2. METHODS

2.1. Pore-scale Lattice Boltzmann-based reactive transport model

The simulator used in this study to perform the reactive transport simulations is based on the Lattice Boltzmann (LB) method, which solves the Navier-Stokes and advection-diffusion-reaction equations. The chemical reaction calculations are performed by PHREEQC[38], which has been coupled with the transport solver. The governing equations of the LB method and the details of the model implementation are given in SI.

2.2. Shale geometries

The pore-scale reactive transport simulations are performed for the 2D and 3D shale geometries (Figures S1-S7). For the 2D shale geometries, two shale samples with the same calcite content but different calcite spatial distribution patterns are generated. These two spatial distributions for calcite are controlled by the two-point correlation function. Two-point correlation is a measure that shows the amount of spatial independence of a single variable at two different points of the studied domain[39]. In other words, this function describes that what is the probability of two different points to have the same value if there is a specific amount of distance between them[39, 40]. When the distance between the two selected points approaches to zero, the probability of them having the same value is at its maximum, while when there is a noticeable gap between the two selected points, their values become almost independent from each other[39, 40]. The domain size of the generated shale geometries is 125μm×125μm with resolution equal to 0.5 μm. To study the effect of the calcite content on the alteration of the shale rocks, one more 2D shale structure with the higher calcite content is also generated. In order to generate the reasonable realizations of the organic-rich shale deposits, we have used some image processing steps that are described as follow. Two Gaussian random files with different standard deviations are interpolated and thresholded to mimic the solid texture of the calcite and silicate minerals[41]. Then, using the watershed segmentation, we have separated the connected elements of calcite and silicate to give them a more grain-like shape[42]. Afterwards, parts of the remaining void space is filled with the clay flakes by thresholding a distance map and adding some levels of noise to imitate a texture of the packed flakes. The remaining void space is assumed to be filled with the porous organic matter, which is called kerogen. Then, some parts of the whole structure is randomly snipped to be embedded by the pyrite framboids as they technically form after the initial deposition of the shale layers[42]. Finally, while knowing the physically stronger parts of the shale structure that are composed of the pure solid minerals, calcite, silicate, and pyrite, we perform a heuristic fracturing simulation in the three directions: horizontal, 45° and 135°. Same procedure were used to generate a 3D shale realization with domain size 125μm×125μm×15μm. The details of the fracturing technique are described in the work performed by Rabbani et al.[43].

3. Simulation setup

The reactions considered in the simulations are the calcite and pyrite dissolution and the barite precipitation. These are some of the commonly observed reactions taking place during the HFF-shale interactions[8, 21, 22, 24]. Simulations are performed for the shales with coarse and fine calcite fragments, designated as CCS and FCS, respectively. To assess the alteration of the shale sample when the calcite content is higher, we simulate a case with the higher calcite in the shale matrix, designated as HCS. For the case of the CCS, we also run a simulation with the higher fluid flowrate to evaluate the effect of transport conditions (more advective transport) on the evolution of shale structure. Calcite contents for the CCS and FCS are the same and equal to ~30%, while the calcite content for HCS is ~63%. The average velocities in the domain for the CCS, FCS, and HCS are 6.66×10^{-7} [$m.s^{-1}$], 8.08×10^{-7} [$m.s^{-1}$], and 8.01×10^{-7} [$m.s^{-1}$], respectively. The average velocity of the simulations for CCS with higher injection velocity is 6.66×10^{-5} [$m.s^{-1}$]. We model the flow of an acidic solution, with pH=2, through the fractured shale geometries. The injected fluid is supersaturated with respect to barite, with SI of 1.3. Therefore, the main source of barium and sulfate for the barite precipitation is derived from the injected solution and not from the host rock. The HFF can have high concentration of barium and sulfate if produced waters are diluted and used as the HFF[8]. The injected HFF composition is given in Table S1. Preliminary simulations showed that the reaction rate of the minerals such as silicate and clay are much slower than calcite during the simulation time scale. Therefore, in the simulations, we treated silicate, clay, and kerogen as non-reactive phases and only calcite, pyrite, and barite were considered as the reactive minerals.

The reaction rates of calcite, pyrite, and barite reactions are calculated based on the following equations[44-46]:

$$\mathrm{R_{calcite}[mol.\,m^{-2}.\,s]} = \left(10^{-0.3}\mathrm{a_{H^+}} + 10^{-5.81} + 10^{-3.48}\mathrm{a}_{\mathrm{H_2}CO_3^*}\right)(1-\Omega_{\mathrm{calcite}}) \tag{1}$$

$$\mathrm{R_{pyrite}[mol.\,m^{-2}.\,s]} = (10^{-8.19}\mathrm{a_{H^+}}^{-0.11}\mathrm{a_{O_2}}^{0.5})(1-\Omega_{\mathrm{pyrite}}) \tag{2}$$

$$\mathrm{R_{barite}[mol.\,m^{-2}.\,s]} = (10^{-6.9}\mathrm{a_{H^+}}^{0.22} + 10^{-7.9})(1-\Omega_{\mathrm{barite}}) \tag{3}$$

where $\mathrm{R_m}$ is the reaction rate of mineral m, $\mathrm{a_i}$ is the activity of the species i, and Ω_m is the saturation ratio of the mineral m. To calculate the amount of the minerals in [mol], the $\mathrm{R_m}$ should be multiplied by the timestep and also the reactive area of the minerals. In the LB method used in this study, the reactive area is computed based on the number of the faces of a solid grid cell which is in contact with fluid.

The fluid composition at the inlet is kept constant during the simulations and it is assumed that the initial fluid composition is the same as the inlet. When solving the mass transfer equation, the no-flow boundary conditions are utilized at the top and the bottom of the domain whereas the zero diffusive-flux boundary condition is applied at the domain outlet. The diffusion coefficient of the chemical species is taken to be the same and equal to 10^{-9} [$m^2.s^{-1}$]. The fluid flow is driven by applying a constant pressure gradient across the domain. The value of the dynamic viscosity used for the fluid is 10^{-6} [$m^2.s^{-1}$].

We look at the different properties of the system such as the fluid chemistry, the mineral distributions, and the porosity-permeability relation in order to evaluate the impacts of the calcite spatial distribution, the calcite content, and the injection flowrate on the structural evolution of the shale samples.

4. RESULTS AND DISCUSSION

4.1. 2D simulations

4.1.1. Effect of calcite spatial distribution and flow velocity

In our simulations, we focused only on the pore-scale spatial distribution of calcite because it is highly reactive under acidic conditions and its reaction rate is faster than other minerals. Different calcite spatial distribution in shale matrices can therefore lead to the different patterns of the microstructural changes in shales. In what follows, we investigate what effluent chemistry, porosity-permeability relations, and mineral distributions look like when the HFF is injected into the CCS and FCS. Moreover, we also assess how a higher flow velocity influences the fluid chemistry, porosity-permeability relations, and mineral profile during HFF-shale interactions. To this end, we run another simulation for the CCS where the initial average velocity in the domain is 6.66×10^{-5} [m.s^{-1}].

Fluid chemistry. Figure 1 shows the temporal evolution of the probability distribution function (PDF) of the pH for the CCS and FCS. Initially at t=0.02[s], the PDFs indicate a peak at low pH values, which reveals that most of the regions in the domain have low pH. Over time, the low pH solution reacts with calcite and this causes the pH to rise (Ca^{2+} level also increases as result of the calcite dissolution; See Figure S8). The increase in the pH is evident from Figure 1, at t=0.05[s] and 0.2[s], where it demonstrates that the peaks at the low pH values are attenuated and a broader range for the pH can be observed. This increase in the pH, which is because of the calcite dissolution, is similar to what was observed during the HFF-shale reactions in the previous experiments[8]. After t=2.0[s], the PDFs in Figure 1 show a peak at higher pH values, indicating that most part of the domain have now pH values greater than 5. This peak moves towards the higher pH values as simulations proceed further. During the later times of the simulation, in addition to the large peak at the higher pH, a small peak at the lower pH starts growing, which represents the regions near the inlet where the low pH HFF, with pH=2, is injected into the domain.

Figure 1 also demonstrates that generally the peaks at the higher pH values for the FCS are larger than that of the CCS. The difference between these peaks becomes smaller as the simulation time approaches t=76[s]. One reason for this difference is that the reactive surface area of calcite in contact with the HFF for the FCS is larger than calcite reactive surface area for the CCS. This can be observed in Figure 2 where it indicates that the total surface area of calcite for the FCS is larger than the calcite reactive area for the CCS.

As can be observed in Figure 1, after t=20.0[s], the change in the pH for the CCS and FCS is not significant. This is because the calcite saturation index, SI_{clcite}, in the domain is approaching zero over time (see Figure S9), implying that the solution is becoming saturated with respect to calcite, thus slowing down the calcite dissolution rate and the pH change. This is consistent with the results from prior experiments reporting that the SI_{clcite} approaches zero[8]. For the CCS with higher velocity, however, a different trend can be observed. As Figure 1 presents, after t=20.0[s], the number of regions in the domain, having a low pH, increases and a peak at the low pH appears in Figure 1 at t=76.0[s]. Figure S9 also reveals that the SI_{clcite} for the case of the CCS with higher velocity is still well below zero for different parts of the domain. This lower pH and lower SI_{clcite} results from the higher velocity of the flow, which reduces the residence time of the HFF in the domain and the low HFF at the inlet flows deeper into the domain and lowers the pH.

In addition to calcite, pyrite also dissolves, releasing more Fe^{2+} into the solution (See Figure S10). The amount of Fe^{2+} produced for the FCS is generally higher than that for the CCS. This could be explained by the difference in the pH for these two cases. As observed in Figure 1, the pH for the FCS is generally higher than the CCS, which according to the pyrite reaction rate equation (Equation 2), causes higher dissolution rate for pyrite and hence higher Fe^{2+}concentrations for the FCS. For the CCS with higher velocity, the Fe^{2+} concentration is generally lower than the FCS and CCS, especially at the later simulation times. This is because the inlet solution, which is lacking any Fe^{2+}, flows faster into the domain and flushes out the produced Fe^{2+} and it decreases the Fe^{2+} concentration.

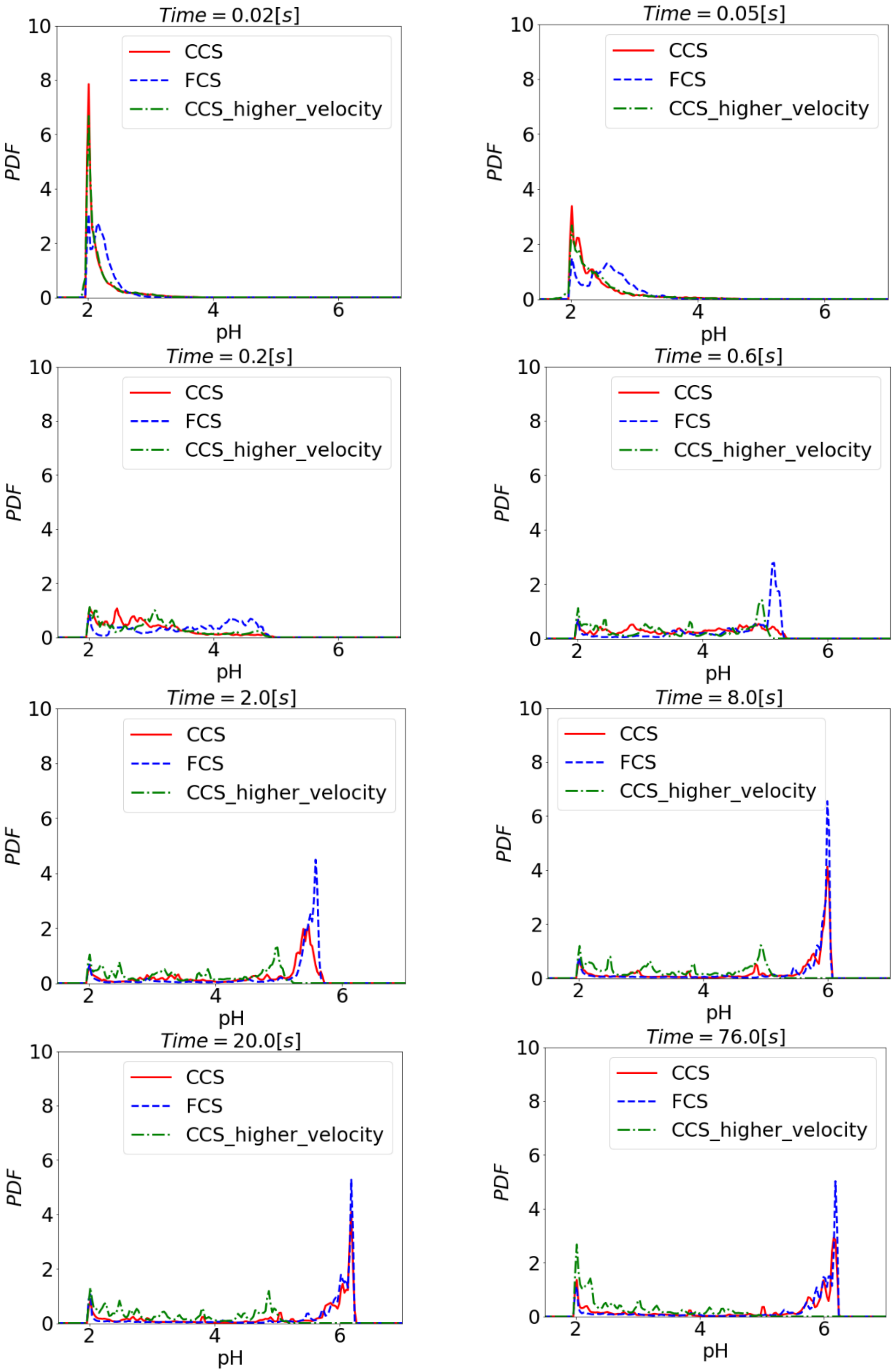

Figure 1. The temporal evolution of the probability distribution function (PDF) of the pH for the CCS (the shale with coarse calcite grains), FCS (the shale with fine calcite grains), and CCS with higher velocity. Over time, the pH in the domain increases because of the calcite dissolution. The number of regions having higher pH values are larger for the FCS compared to other cases. The case of the CCS with higher velocity generally shows lower pH values which is due to the short residence time of the HFF in the domain.

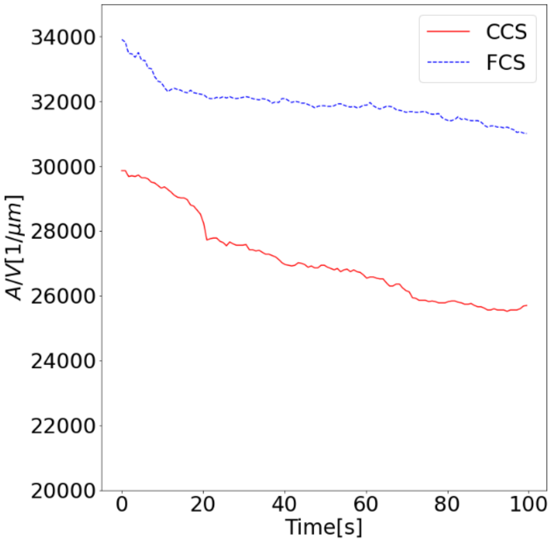

Figure 2. the temporal changes of the total reactive surface area of the calcite grains, in contact with the HFF, for the CCS and FCS.

Mineral reaction patterns. As Figures 3 shows, most of the calcite dissolution in the shales occurs close to the inlet, where the pH is the lowest, and most of the calcite (grey color in Figure 3) in the other parts of the domain remain unaltered. This dissolution pattern is similar to the face dissolution patterns, which usually happen at the low Peclet numbers[47]. For the case of the CCS with higher velocity, greater calcite dissolution along the flow direction can be observed. As presented in Figure 3, Contrary to calcite, pyrite does not show any geometry evolution. Pyrite does react with the HFF, as the Fe^{2+} concentration confirms this (Figure S10), but the complete dissolution of the pyrite grains is not detectable during the timescale of the simulations. The slow reaction rate of pyrite is due to the lack of high concentrations of dissolved O_2 in the influent.

The injected acidic solution is supersaturated with respect to barite. Barite therefore precipitates on the surfaces of the minerals present in the shales. In this study, we simulate the barite nucleation by assigning initial seeds or nuclei to all the substrates where these nuclei initiate the barite growth. The heterogeneous nucleation of barite therefore occurs on all the substrates once the supersaturated solution is in contact with a mineral substrate. Figure 3 also presents the distribution of the precipitated barite in the system for the FCS and CCS. As the simulation proceeds, more barite precipitate in the areas close to the inlet because of the access to the solution that is more supersaturated with respect to barite. It is evident that, for the FCS, barite has mostly precipitated near the inlet whereas for the CCS, the barite precipitation front has penetrated into the domain, which is because of the calcite dissolution. The depth of penetration is even more when the supersaturated solution is injected at a higher velocity. This pattern is qualitatively similar to the barite precipitation patterns observed in previous studies[22] where they have shown that for the calcite-rich Eagle ford shale samples, the barite precipitation front has extended into the shale matrix in contrast to the low calcite content Marcellus shale where the barite precipitation front is mainly limited at the HFF-matrix interface. It should be pointed out that in our study, we observe more barite precipitation into the domain for the CCS shale because calcite dissolves and it provides a new porosity. The supersaturated solution can therefore penetrate more into the domain and thus barite can precipitate further down the domain. In the prior studies[24], however, the greater amount of barite precipitation into the shale matrix, observed for the calcite-rich shale, has been attributed to the effect of the higher pH on the deprotonation of HSO_4^-. It is reported that HSO_4^- is deprotonated at the near-neutral conditions, thus increasing the SO_4^{2-} concentration, which leads to a higher rate for the barite precipitation[22].

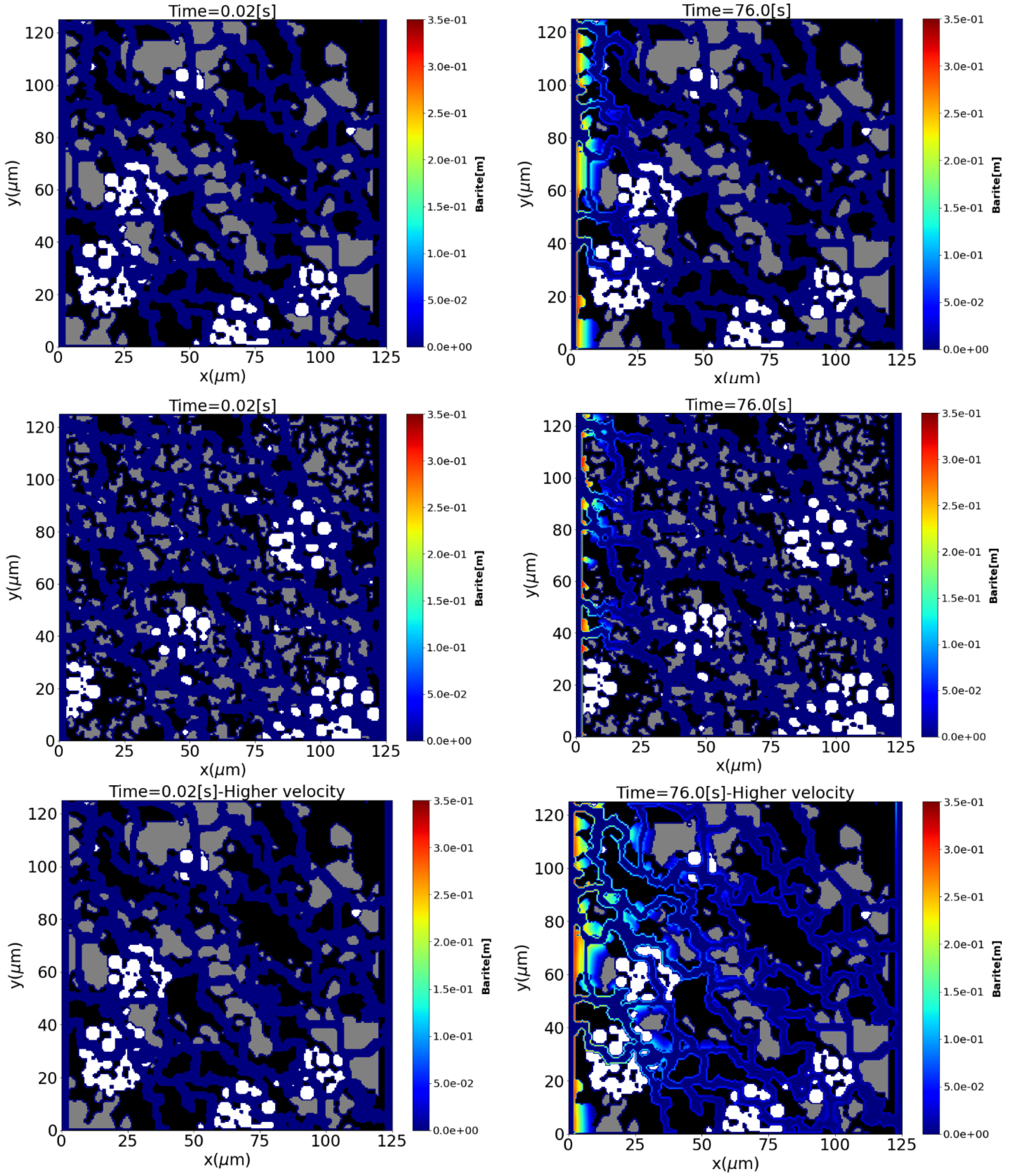

Figure 3. The amount of barite precipitated at 0.02[s] (left column) and 76[s] (right column) for the CCS (first row), the FCS (middle row), and the CCS with higher velocity (last row). In the plots, Grey colour denotes calcite, black colour denotes non-reactive minerals, and white colour denotes pyrite. Over time, few calcite surfaces near the inlet dissolve. While pyrite reacts with the HFF, its geometry evolution is not visible during the simulation time scale. As shown, little barite precipitation occurs near the inlet where the influent solution is more supersaturated with respect to barite. For the CCS, barite precipitation extends further into the domain and increasing the velocity increases this penetration depth.

Porosity-permeability relationship. The calcite dissolution and the barite precipitation change the porosity and the permeability of the shale samples. Figure 4 represents the normalized permeability (permeability/initial permeability) and porosity (porosity/initial porosity) versus time and also the normalized permeability versus the normalized porosity for the CCS, FCS, and CCS with higher velocity. The permeability values for the shales were calculated by using the velocity profile. As evident from Figure 4, the permeability and the porosity of the shales increase over time. Overall, the permeability values for the CCS are higher than that for the FCS. For the CCS, the dissolution of calcite grains plays a more important role in increasing the permeability since the calcite grains are coarser and their dissolution leads to higher porosities and permeabilities, whereas for the FCS, the grains are generally finer and their dissolution does not change the permeability as much as the dissolution of the coarser grains. As observed in Figure 3, increasing the flow velocity leads to greater dissolution of calcite grains along the flow direction and this translates into higher permeabilities for the case of the CCS with higher velocity.

As simulations proceed, the solution inside the domain tends to become saturated with respect to calcite, meaning that the calcite dissolution rate decreases. This also slows down the rate of the permeability enhancement, which is clearly shown in Figure 4 at the later simulation times. This observation is not completely valid for the CCS with higher velocity because, as Figure S9 shows, the solution in the domain is still undersaturated with respect to calcite and has the capacity to dissolve more calcite and increases the permeability further.

It should be mentioned that during the simulations, although barite is precipitating, it has not yet contributed to the porosity and permeability of the shales as none of the simulation grid cells, in which barite is precipitating, has been completely filled with barite so that the cell can be considered as a solid grid cell. The current model can indeed account for simultaneous dissolution and precipitation to occur. This means that we could then expect to see a more dynamic porosity-permeability relationship due to coexistence of the calcite dissolution and the barite precipitation. To be able to see this dynamic porosity-permeability relationship, the simulations would need to be run for longer times, which will be the focus of our future endeavor.

4.1.2. Effect of calcite content

Previous experimental studies have shown that the different calcite contents in shale matrices can lead to different microstructural changes in shales[21, 22]. This section will therefore deploy the built reactive transport model to assess how a different calcite content influences the alteration of the shale rock. To this end, we compare the results (fluid chemistry, porosity-permeability relations, and mineral profiles) from the CCS simulations with the ones from the HCS (having higher calcite content) simulations.

Fluid chemistry. A higher calcite content in the shale matrix will generally results in higher pH values as demonstrated in Figure 5. At the early times during the simulation, the pH in the domain is between 2 and 3. During the later times, most parts of the domain exhibit pH values greater than 5.5. As can be observed in Figure 5, at any given time, the HCS shows higher pH values, which is clearly because of its higher calcite content. For the HCS, this higher calcite content also causes the solution to have a higher $SI_{calcite}$ (see Figure S11) due to the greater buffering capacity. The higher pH, produced in the case of the HCS, also causes greater Fe^{2+} to be released into the solution, which is reflected as higher peaks of Fe^{2+} in Figure S12.

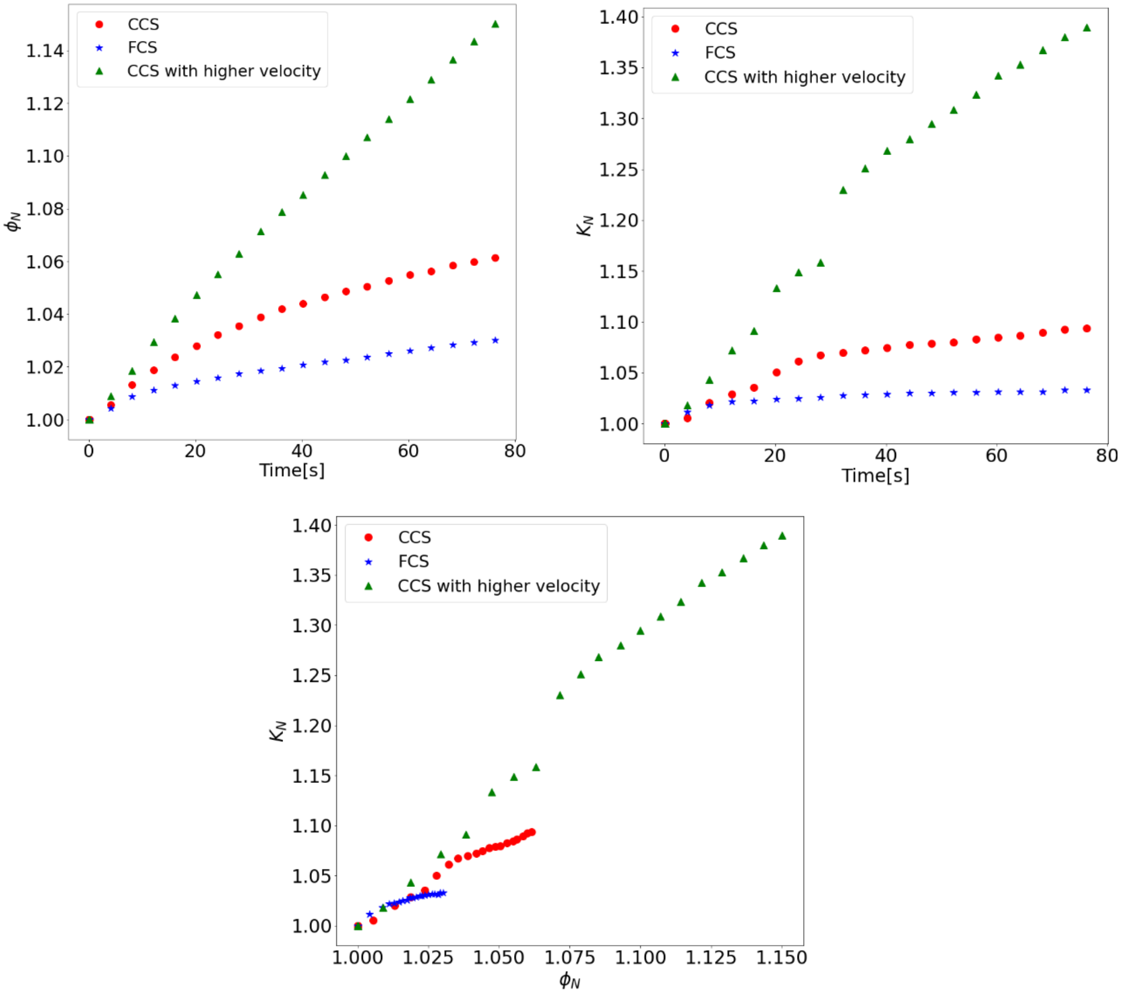

Figure 4. The plots of the Normalized permeability versus time, normalized porosity versus time, and the normalized permeability versus normalized porosity for the CCS, FCS, and CCS with higher velocity. As shown, the permeability values of the CCS are higher than the FCS, which is clearly because of greater extent of the calcite dissolution occurred for the CCS. Increasing the velocity leads to the higher permeabilities because greater calcite dissolution takes place when velocity is higher and the residence time of the HFF is shorter in the domain.

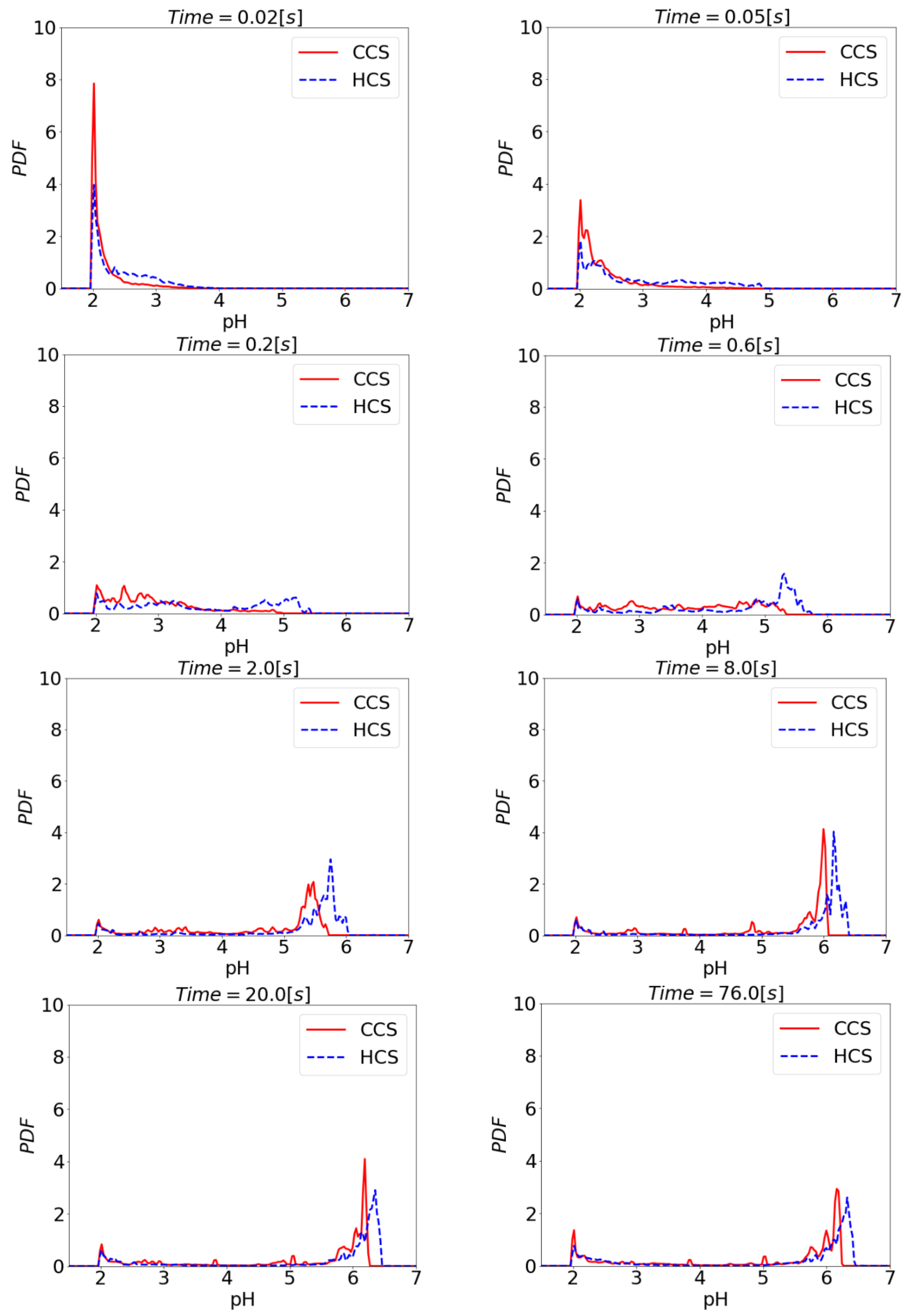

Figure 5. The temporal evolution of the probability distribution function (PDF) of the pH for the CCS (the shale with coarse calcite grains) and the HCS (the shale with higher calcite content). Over time, the pH in the domain increases because of the calcite dissolution. Since the HCS has higher calcite content, it generally exhibits higher pH values.

Mineral reaction patterns. Figure 6 reveals that most of the calcite dissolution occurs near the inlet where the pH of HFF is low. In both the CCS and HCS, the location of the calcite dissolution front is almost the same. This is also valid for the barite precipitation front; in both cases the penetration depth of the barite precipitation is the same. However, as simulations proceed, both the location of the calcite dissolution and barite precipitation fronts for the HCS will extend further because there are more calcite grains that can dissolve and consequently their dissolution allow the barite precipitation to move towards the outlet.

Another feature observed when barite precipitates is that the amount of barite precipitated on the non-reactive minerals is higher compared to the amount of barite precipitated on calcite (see the area surrounded by the red circle in Figure S13 for a comparison of the amount of barite precipitated on calcite and the non-reactive minerals). This is because the solution near the non-reactive minerals have a lower pH whereas the solution close to calcite has a higher pH caused by the calcite dissolution. The barite rate expression, used in this study, has an inverse relation with the pH meaning that when the pH is lower, the barite precipitation rate will be higher. This is also consistent with the previous studies showing that the barite precipitation rate is high at acidic conditions[48].

Figure 6 also shows no significant pyrite dissolution as its dissolution rate is very slow considering the limited amount of dissolved oxygen in the influent.

Porosity-permeability relationship. Figure 7 presents the results of the evolution of the normalized permeability and normalized porosity for the CCS and HCS. At any given time, the normalized permeability and normalized porosity for the HCS are higher than that for the CCS because the HCS have a higher calcite content which leads to greater calcite dissolution and consequently to higher porosity and permeability values. As evident from Figure 7, the normalized porosity and normalized permeability initially experience a rather sharp increase but later the rate of change in K_N and $\emptyset_N$ slows down which is due to the reduction in calcite dissolution rate. This reduction is less pronounced for the HCS because there are more calcite grains near the inlet and they can react with the acidic solution to create more porosity, which can also increase the permeability. The K_N vs $\emptyset_N$ plot in Figure 7 indicates that for a given $\emptyset_N$, the CCS exhibits a higher K_N than the HCS. This is because the time it takes for the CCS to reach to a certain $\emptyset_N$ is longer than that for the HCS. The HCS has a higher calcite content and it can therefore reach to that certain $\emptyset_N$ by dissolving the greater amount of calcite within a shorter period of time. During this shorter time period, the K_N for the HCS still has not increased as much as that for the CCS.

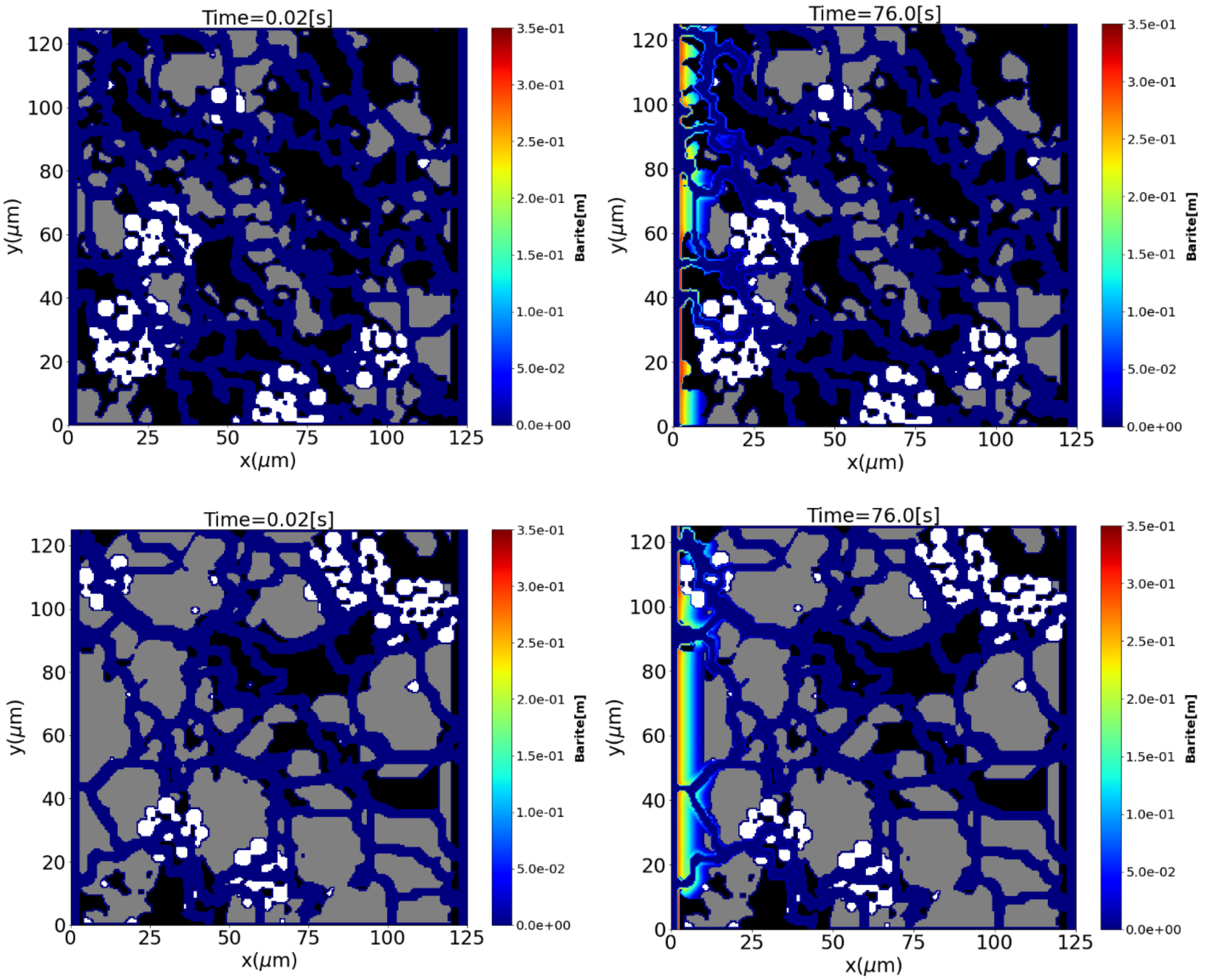

Figure 6. The amount of barite precipitated at 0.02[s] (left column) and 76[s] (right column) for the CCS (first row) and the HCS (middle row). In the plots, Grey colour denotes calcite, black colour denotes non-reactive minerals, and white colour denotes pyrite. Over time, few calcite surfaces near the inlet dissolve. While pyrite reacts with the HFF, its geometry evolution is not visible during the simulation time scale. As shown, little barite precipitation occurs near the inlet where the influent solution is more supersaturated with respect to barite. For the HCS, the extent of barite precipitation is more than the CCS.

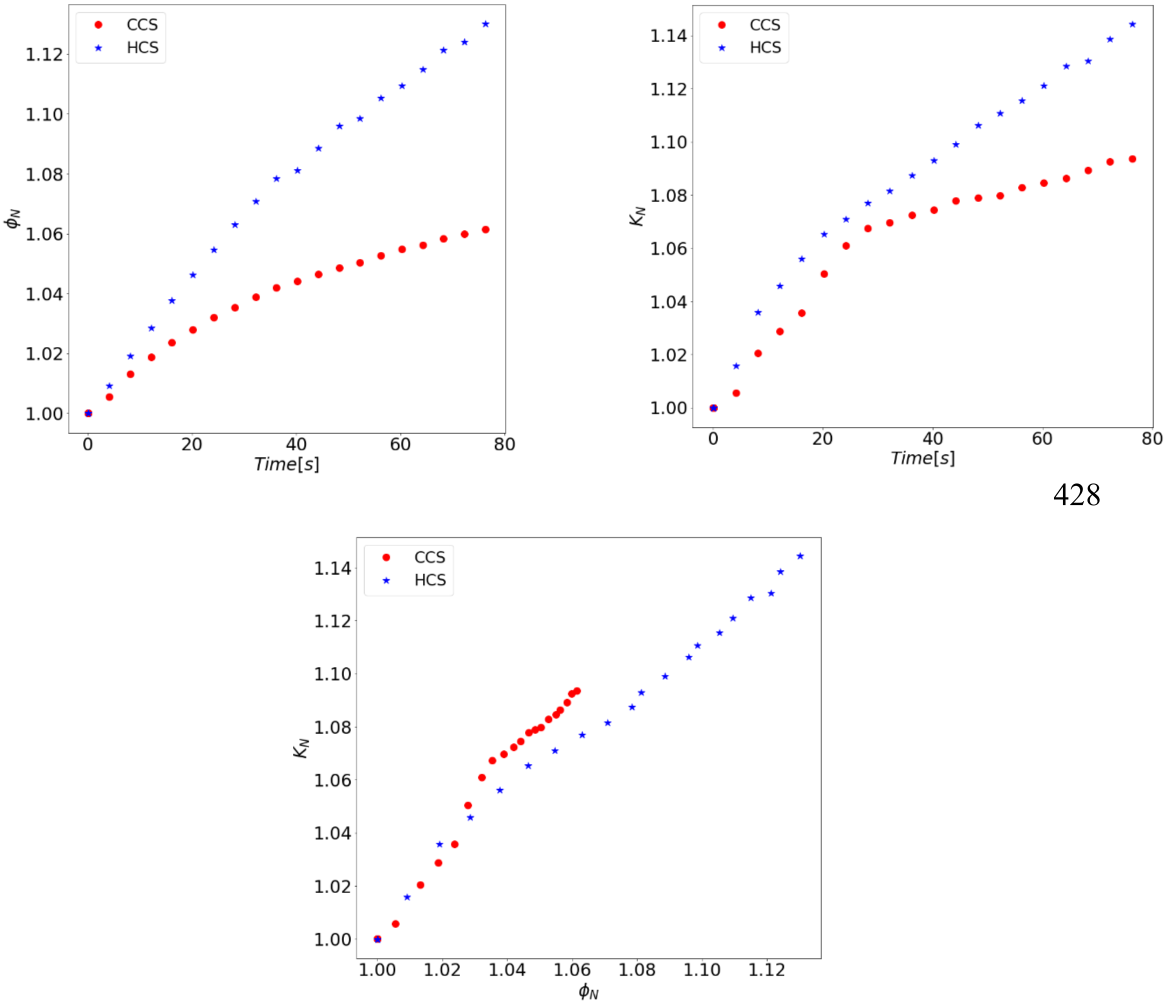

Figure 7. The plots of the Normalized permeability versus time, normalized porosity versus time, and the normalized permeability versus normalized porosity for the CCS and HCS. As shown, the permeability values of the HCS are higher than the CCS at any given time, which is clearly because of greater extent of the calcite dissolution occurred for the HCS. In the normalized permeability versus normalized porosity, for a given normalized porosity, the normalized permeability of the CCS is higher than that for the HCS. This is because it takes more time for the CCS to reach to a certain porosity and at this longer time, the CCS has a higher normalized permeability compared to the HCS, for which it takes shorter time to reach to the same normalized porosity.

4.2. 3D simulations

Compared to the 2D simulations, simulations on the 3D shale geometry might provide better insights into the shale and the HFF chemical interactions as the reactive transport processes are modelled in 3D. To this end, we perform the 3D simulations and present some of the preliminary results related to the calcite dissolution and the barite precipitation in the 3D shale geometry in the early times during the simulations. The aim here is to show the capability of the pore-scale model to handle and simulate 3D geometries. This 3D model will be used in a future work to provide inputs for a multiscale reactive transport model. The pore-scale model can provide the local, or the small-scale, information for the multi-scale reactive transport simulators. Due to the existence of multiple length-scales in the shale reservoirs, the multiscale models are a better choice for simulating the large-scale reactive transport processes in comparison with using only the pore-scale or only the continuum scale models. In the development of the multiscale models, the information related to the smaller scales needs to be incorporated into the multi-scale models. This information of the small-scale can be provided by experiments[49] or perhaps more easily by the pore-scale reactive transport modeling as developed in this study.

For the 3D simulations, all the flow and the concentration boundary conditions remain the same as for the 2D simulations. In the following we show the preliminary results of the analyses performed for the 3D simulation.

Figure 8 demonstrates the Ca^{2+} concentration profile at t = 0.02s and 6s. The increase in Ca^{2+} concentration at t=6s confirms the calcite dissolution reaction, which is also clear from the temporal evolution of the effluent Ca^{2+} concentration (Figure 9a). The effluent Ca^{2+} data in the 3D simulation also shows a plateau after an initial rather sharp increase in the effluent Ca concentration. The fluid pH level in the domain also starts to rise as the result of the calcite dissolution as is evident from Figure S14 where pH has increased from initial value of 2 to higher values. Figure 9b also shows the effluent pH in the shale where it indicates that the pH has been buffered. It is evident from Figure 9b that the pH becomes stabilized over time, which is probably because of a reduction in the calcite dissolution rate in areas where the transport becomes diffusion dominated.

The barite precipitation pattern for the 3D shale geometry is presented in Figure 10. Here calcite, pyrite, and the non-reactive minerals are not shown to enable a better observation of the barite precipitated in the system. At t = 0.02s, barite has precipitated uniformly everywhere in the domain (Figure 10) because the initial solution is supersaturated with respect to barite and it has been assumed that the barite heterogeneous nucleation occurs on all the solid substrates (calcite, pyrite and the non-reactive minerals). At t = 6s, the extent of the barite precipitation decreases towards the outlet. The reason is that the regions near the inlet have access to the more fresh solution with the higher supersaturation with respect to barite and this causes the more heterogeneous barite precipitation close to the inlet.

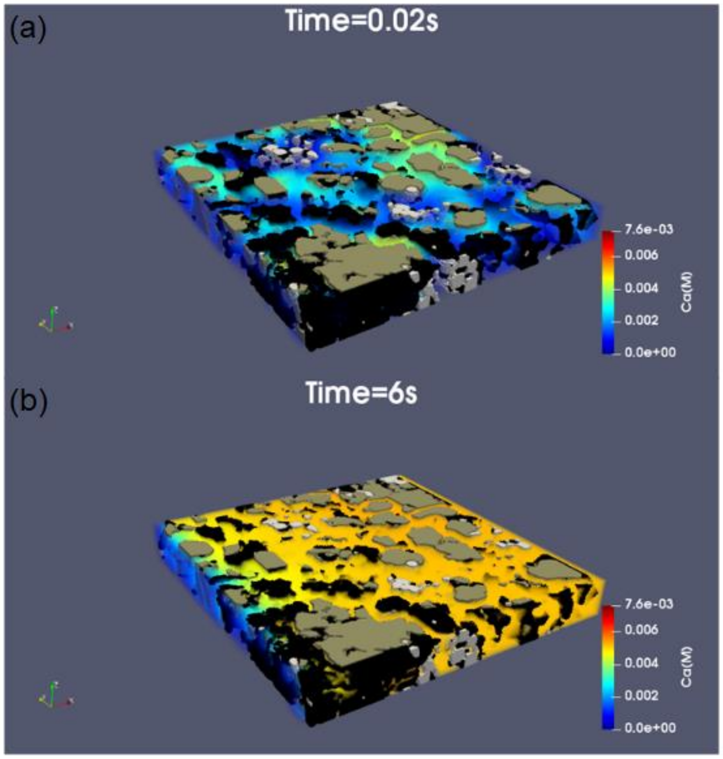

Figure 8. The Ca^{2+} concentration profile for the 3D simulation at t = 0.02s and 6s. In the plots, Grey colour denotes calcite, black colour denotes the non-reactive minerals, and white colour denotes pyrite. At t = 0.02s, the higher Ca^{2+} concentration around the calcite surfaces indicates the calcite dissolution. At t=6s, the Ca^{2+} concentration has increased in most parts of the domain because of the further calcite dissolution and the transport of Ca.

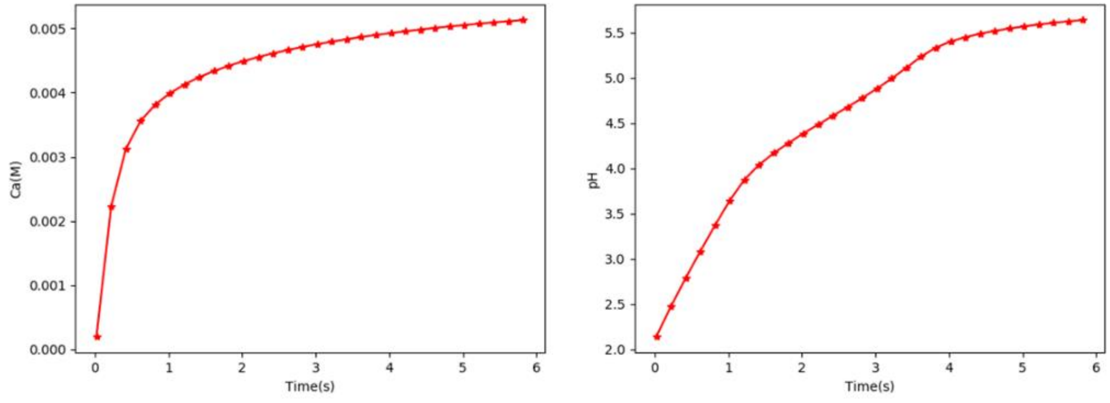

(a) (b)

Figure 9. (a) Temporal evolution of the effluent Ca^{2+} concentration for the 3D simulation. Early in the simulation, the Ca^{2+} concentration shows a sharp increase, which is followed by a more stabilized trend caused by decreasing the calcite dissolution rate. (b) Temporal evolution of the effluent pH for the 3D simulation. As shown, the effluent pH increases as the result of the calcite dissolution and this increasing trend seems to become stabilized over time.

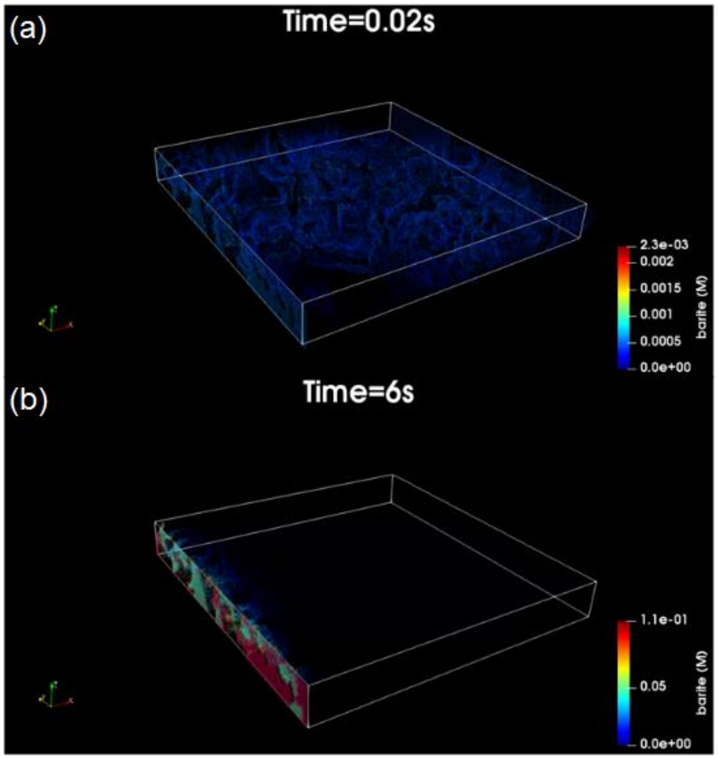

Figure 10. The amount of barite precipitated in the 3D shale sample at t=0.02s and t=6s. The minerals are removed from the figure to facilitate the better observation of the barite precipitation. At t=0.02s, a uniform barite precipitation pattern can be observed in the entire domain. At t=6s, more barite precipitate near the inlet where the solution has a higher supersaturation with respect to barite.

5 CONCLUSIONS

We build the 2D and the 3D pore-scale reactive transport models to better understand how geochemical interactions between fracturing fluid and shale rock impact the transport properties of the shale rocks. In particular, we study the effect of the pore-scale calcite distribution on the evolution in structure of representative shales when a fracturing fluid flows through fractured shale structures. Some of the 2D simulations were performed on two different shales with different calcite pore-scale distribution. The simulations were also carried out for the scenarios with higher flowrates.

We found from the 2D simulations that during the HFF-shale chemical interactions, the shale rock with the finer calcite grains exhibits higher pH values compared to the shale rock composed of the same amount of calcite but with the coarser grain sizes. Results also showed that the injection of the HFF with a higher velocity/rate results in lower pH values because of the shorter residence time for the HFF in the domain.

The injected HFF was supersaturated with respect to barite, so barite precipitation occurred during the simulations. For the shale composed of the fine grains of calcite, barite precipitation mostly occurred near the inlet, but for the shale having coarser grains of calcite, the barite precipitation extended further down the domain. The results also demonstrated that injection of the HFF with higher velocity causes the barite precipitation front to extend more into the domain.

The results revealed that the permeability increase, triggered by calcite dissolution, is higher for the shale sample with the coarser calcite grains. This may be due to the emergence of more (and possibly larger) pathways made available by the dissolution in the samples with the larger calcite grains. We also found that the higher flowrate increases the permeability enhancement.

The 2D simulations were also run to study the effect of the calcite content on the alteration of the shales. The analysis of the fluid chemistry indicated that the samples with the higher calcite content can neutralize the acid pH (because of more calcite dissolution) faster than those with the lower calcite content. Results also showed that for samples with the higher calcite content, the extent of barite precipitation in the shale rock is higher compared to the samples with the lower calcite content. This allows us to predict the long-term evolution of the transport properties during the fracturing process due to clogging.

We also showed the ability of the developed model to tackle the 3D simulations. Some preliminary 3D simulations of the HFF-shale interaction were presented. The 3D model will be used in our future work to provide inputs for upscaling methods such as the upscaling techniques[49] used to obtain continuous time random walk (CTRW) parameters at larger scales. This allows upscaling of reactive transport processes from pore-scales to larger scales.

ASSOCIATED CONTENT

Supporting Information

The supporting information is available free of charge.

Description of the pore-scale reactive transport solver; figures showing the 2D and 3D mineralogy of the shales; figures indicating the PDFs of the $SI_{calcite,}$ Ca^{2+} and Fe^{2+} for the CCS, FCS, HCS, and CCS with higher velocity; figures indicating the pH and the barite precipitated for the HCS at time=1[s];figures indicating pH and velocity profiles for 3D simulations;

AUTHOR INFORMATION

CORRESPONDING AUTHOR

H.Fazeli@hw.ac.uk

ACKNOWLEDGMENT

This work was supported by the Natural Environment Research Council (grant number NE/R018030/1) which is gratefully acknowledged.

REFERENCES

1. Kargbo, D. M.; Wilhelm, R. G.; Campbell, D. J., Natural gas plays in the Marcellus Shale: challenges and potential opportunities. ACS Publications: 2010.

2. Soeder, D. J.; Kappel, W. M., *Water resources and natural gas production from the Marcellus Shale*. US Department of the Interior, US Geological Survey Reston, Virginia: 2009.

3. Andrews, I. J., The Carboniferous Bowland Shale gas study: geology and resource estimation. **2013**.

4. Herrmann, J.; Rybacki, E.; Sone, H.; Dresen, G., Deformation Experiments on Bowland and Posidonia Shale—Part I: Strength and Young's Modulus at Ambient and In Situ p c–T Conditions. *Rock Mechanics and Rock Engineering* **2018,** *51* (12), 3645-3666.

5. Herrmann, J.; Rybacki, E.; Sone, H.; Dresen, G., Deformation Experiments on Bowland and Posidonia Shale—Part II: Creep Behavior at In Situ pc–T Conditions. *Rock Mechanics and Rock Engineering* **2020,** *53* (2), 755-779.

6. Harrison, A. L.; Jew, A. D.; Dustin, M. K.; Thomas, D. L.; Joe-Wong, C. M.; Bargar, J. R.; Johnson, N.; Brown Jr, G. E.; Maher, K., Element release and reaction-induced porosity alteration during shale-hydraulic fracturing fluid interactions. *Applied geochemistry* **2017,** *82*, 47-62.

7. Jew, A. D.; Dustin, M. K.; Harrison, A. L.; Joe-Wong, C. M.; Thomas, D. L.; Maher, K.; Brown Jr, G. E.; Bargar, J. R., Impact of organics and carbonates on the oxidation and precipitation of iron during hydraulic fracturing of shale. *Energy & Fuels* **2017,** *31* (4), 3643-3658.

8. Paukert Vankeuren, A. N.; Hakala, J. A.; Jarvis, K.; Moore, J. E., Mineral reactions in shale gas reservoirs: Barite scale formation from reusing produced water as hydraulic fracturing fluid. *Environmental science & technology* **2017,** *51* (16), 9391-9402.

9. Dieterich, M.; Kutchko, B.; Goodman, A., Characterization of Marcellus Shale and Huntersville Chert before and after exposure to hydraulic fracturing fluid via feature relocation using field-emission scanning electron microscopy. *Fuel* **2016,** *182*, 227-235.

10. Liu, D.; Li, Y.; Agarwal, R. K., Numerical simulation of long-term storage of CO2 in Yanchang shale reservoir of the Ordos basin in China. *Chemical Geology* **2016,** *440*, 288-305.

11. Wang, L.; Fortner, J. D.; Giammar, D. E., Impact of water chemistry on element mobilization from Eagle Ford Shale. *Environmental Engineering Science* **2015,** *32* (4), 310-320.

12. Wilke, F. D.; Vieth-Hillebrand, A.; Naumann, R.; Erzinger, J.; Horsfield, B., Induced mobility of inorganic and organic solutes from black shales using water extraction: Implications for shale gas exploitation. *Applied Geochemistry* **2015,** *63*, 158-168.

13. Barbot, E.; Vidic, N. S.; Gregory, K. B.; Vidic, R. D., Spatial and temporal correlation of water quality parameters of produced waters from Devonian-age shale following hydraulic fracturing. *Environmental science & technology* **2013,** *47* (6), 2562-2569.

14. Kekacs, D.; McHugh, M.; Mouser, P. J., Temporal and thermal changes in density and viscosity of Marcellus shale produced waters. *Journal of Environmental Engineering* **2015,** *141* (12), 06015006.

15. Marcon, V.; Joseph, C.; Carter, K. E.; Hedges, S. W.; Lopano, C. L.; Guthrie, G. D.; Hakala, J. A., Experimental insights into geochemical changes in hydraulically fractured Marcellus Shale. *Applied Geochemistry* **2017,** *76*, 36-50.

16. Tasker, T. L.; Piotrowski, P. K.; Dorman, F. L.; Burgos, W. D., Metal associations in Marcellus shale and fate of synthetic hydraulic fracturing fluids reacted at high pressure and temperature. *Environmental Engineering Science* **2016,** *33* (10), 753-765.

17. Pilewski, J.; Sharma, S.; Agrawal, V.; Hakala, J. A.; Stuckman, M. Y., Effect of maturity and mineralogy on fluid-rock reactions in the Marcellus Shale. *Environmental Science: Processes & Impacts* **2019,** *21* (5), 845-855.

18. Herz-Thyhsen, R. J.; Kaszuba, J. P.; Dewey, J. C., Dissolution of Minerals and Precipitation of an Aluminosilicate Phase during Experimentally Simulated Hydraulic Fracturing of a Mudstone and a Tight Sandstone in the Powder River Basin, WY. *Energy & Fuels* **2019**.

19. Chen, Q.; Kang, Y.; You, L.; Yang, P.; Zhang, X.; Cheng, Q., Change in composition and pore structure of Longmaxi black shale during oxidative dissolution. *International Journal of Coal Geology* **2017,** *172*, 95-111.

20. Jew, A. D.; Harrison, A. L.; Kiss, A. M.; Dustin, M. K.; Joe-Wong, C.; Thomas, D. L.; Maher, K.; Brown Jr, G. E.; Cercone, D.; Bargar, J. R. In *Mineralogical and Physical Changes that Control Pore-Scale Shale-Gas Properties*, Unconventional Resources Technology Conference (URTEC): 2017.

21. Li, Q.; Jew, A. D.; Kiss, A. M.; Kohli, A.; Alalli, A.; Kovscek, A. R.; Zoback, M. D.; Cercone, D.; Maher, K.; Brown Jr, G. E. In *Imaging Pyrite Oxidation and Barite Precipitation in Gas and Oil Shales*, Unconventional Resources Technology Conference, Houston, Texas, 23-25 July 2018, Society of Exploration Geophysicists, American Association of Petroleum …: 2018; pp 875-884.

22. Li, Q.; Jew, A. D.; Kohli, A.; Maher, K.; Brown Jr, G. E.; Bargar, J. R., Thicknesses of Chemically Altered Zones in Shale Matrices Resulting from Interactions with Hydraulic Fracturing Fluid. *Energy & Fuels* **2019,** *33* (8), 6878-6889.

23. Zhou, Y.; You, L.; Kang, Y.; Cheng, Q.; Zhang, N., Experimental evaluation of oxidation sensitivity in organic-rich shale reservoir. *Journal of Petroleum Science and Engineering* **2020**, 107230.

24. Li, Q.; Jew, A. D.; Brown, J., Gordon E; Bargar, J. R.; Maher, K., Reactive Transport Modeling of Shale-Fluid Interactions after Imbibition of Fracturing Fluids. *Energy & Fuels* **2020**.

25. Cai, Z.; Wen, H.; Li, L., Clay Distribution Patterns Regulate Natural Attenuation of Marcellus Shale Waters in Natural Aquifers. *Energy & Fuels* **2018,** *32* (9), 9672-9682.

26. Li, Y.; Yang, S.; Liu, D.; Yang, C.; Yang, Z.; Li, H.; Tang, Z., Experimental study of shale-fluids interaction during oxidative dissolution with hydrogen peroxide, sodium hypochlorite and sodium persulfate. *Applied Geochemistry* **2020,** *113*, 104503.

27. Osselin, F.; Saad, S.; Nightingale, M.; Hearn, G.; Desaulty, A.; Gaucher, E.; Clarkson, C.; Kloppmann, W.; Mayer, B., Geochemical and sulfate isotopic evolution of flowback and produced waters reveals water-rock interactions following hydraulic fracturing of a tight hydrocarbon reservoir. *Science of The Total Environment* **2019,** *687*, 1389-1400.

28. Pearce, J.; Turner, L.; Pandey, D., Experimental and predicted geochemical shale-water reactions: Roseneath and Murteree shales of the Cooper Basin. *International Journal of Coal Geology* **2018,** *187*, 30-44.

29. Zeng, L.; Reid, N.; Lu, Y.; Hossain, M. M.; Saeedi, A.; Xie, Q., Effect of the Fluid–Shale Interaction on Salinity: Implications for High-Salinity Flowback Water during Hydraulic Fracturing in Shales. *Energy & Fuels* **2020,** *34* (3), 3031-3040.

30. Cai, Z.; Li, L., How long do natural waters "remember" release incidents of Marcellus Shale waters: a first order approximation using reactive transport modeling. *Geochemical transactions* **2016,** *17* (1), 6.

31. Cai, Z.; Wen, H.; Komarneni, S.; Li, L., Mineralogy controls on reactive transport of Marcellus Shale waters. *Science of the Total Environment* **2018,** *630*, 1573-1582.

32. Vilcáez, J., Reactive transport modeling of produced water disposal into dolomite saline aquifers: Controls of barium transport. *Journal of Contaminant Hydrology* **2020**, 103600.

33. Hommel, J.; Coltman, E.; Class, H., Porosity–permeability relations for evolving pore space: a review with a focus on (bio-) geochemically altered porous media. *Transport in Porous Media* **2018,** *124* (2), 589-629.

34. Poonoosamy, J.; Klinkenberg, M.; Deissmann, G.; Brandt, F.; Bosbach, D.; Mäder, U.; Kosakowski, G., Effects of solution supersaturation on barite precipitation in porous media and consequences on permeability: Experiments and modelling. *Geochimica et cosmochimica acta* **2020,** *270*, 43-60.

35. Prasianakis, N.; Curti, E.; Kosakowski, G.; Poonoosamy, J.; Churakov, S., Deciphering pore-level precipitation mechanisms. *Scientific reports* **2017,** *7* (1), 1-9.

36. Seigneur, N.; Mayer, K. U.; Steefel, C. I., Reactive transport in evolving porous media. *Reviews in Mineralogy and Geochemistry* **2019,** *85* (1), 197-238.

37. Vengosh, A.; Jackson, R. B.; Warner, N.; Darrah, T. H.; Kondash, A., A critical review of the risks to water resources from unconventional shale gas development and hydraulic fracturing in the United States. *Environmental science & technology* **2014,** *48* (15), 8334-8348.

38. Charlton, S. R.; Parkhurst, D. L., Modules based on the geochemical model PHREEQC for use in scripting and programming languages. *Computers & Geosciences* **2011,** *37* (10), 1653-1663.

39. Berryman, J. G., Relationship between specific surface area and spatial correlation functions for anisotropic porous media. *Journal of mathematical physics* **1987,** *28* (1), 244.

40. Chen, D.; Teng, Q.; He, X.; Xu, Z.; Li, Z., Stable-phase method for hierarchical annealing in the reconstruction of porous media images. *Physical Review E* **2014,** *89* (1), 013305.

41. Roberts, A. P., Statistical reconstruction of three-dimensional porous media from two-dimensional images. *Physical Review E* **1997,** *56* (3), 3203.

42. Rabbani, A.; Ayatollahi, S., Comparing three image processing algorithms to estimate the grain-size distribution of porous rocks from binary 2D images and sensitivity analysis of the grain overlapping degree. *Special Topics & Reviews in Porous Media: An International Journal* **2015,** *6* (1).

43. Rabbani, A.; Babaei, M.; Javadpour, F., A triple pore network model (t-pnm) for gas flow simulation in fractured, micro-porous and meso-porous media. *Transport in Porous Media* **2020**, 1-34.

44. Fan, W. The Influence of Water-Rock Interaction on Trace Element Mobilization during Shale Gas Production. 2018.

45. Palandri, J.; Kharaka, Y., A compilation of rate parameters of water-mineral interaction kinetics for application to geochemical modeling, USGS Open File report 2004-1068. *Menlo Park, California, National Energy Technology Laboratory–United States Department of Energy* **2004**.

46. Williamson, M. A.; Rimstidt, J. D., The kinetics and electrochemical rate-determining step of aqueous pyrite oxidation. *Geochimica et Cosmochimica Acta* **1994,** *58* (24), 5443-5454.

47. Kang, Q.; Chen, L.; Valocchi, A. J.; Viswanathan, H. S., Pore-scale study of dissolution-induced changes in permeability and porosity of porous media. *Journal of Hydrology* **2014,** *517*, 1049-1055.

48. Ruiz-Agudo, C.; Putnis, C. V.; Ruiz-Agudo, E.; Putnis, A., The influence of pH on barite nucleation and growth. *Chemical Geology* **2015,** *391*, 7-18.

49. Muljadi, B. P.; Bijeljic, B.; Blunt, M. J.; Colbourne, A.; Sederman, A. J.; Mantle, M. D.; Gladden, L. F., Modelling and upscaling of transport in carbonates during dissolution: Validation and calibration with NMR experiments. *Journal of contaminant hydrology* **2018,** *212*, 85-95.

GRAPHICAL ABSTRACT